JOURNAL OF SPACECRAFT AND ROCKETS
Vol. 35, No. 3, May–June 1998

Trajectory-Based Thermal Protection System Sizing for an X-33 Winged Vehicle Concept

David Olynick*
NASA Ames Research Center, Moffett Field, California 94035-1000

A trajectory-based thermal protection system sizing is implemented for an X-33 winged-body vehicle concept. The heat pulse is discretized at eight points along the suborbital trajectory. An aerothermal database is generated from both laminar and turbulent flow calculations. With the aerothermal database and one-dimensional thermal protection system stackups, a number of thermal protection system (TPS) sizings are generated. Three major conclusions from the analysis in this study are as follows: 1) The procedure for performing the TPS mapping works well, 2) for the TPS design, a number of traceability issues exist between the X-33 and the full-scale reusable launch vehicle, and 3) for the X-33 TPS material selection, predictions of transition to turbulence and turbulent heating are critical.

Nomenclature

C_T = heat transfer coefficient, W/m^2-K
c_p = heat capacity of solid
c_s = mass fraction for species s
D = diffusion coefficient, m^2/s
E = activation energy, K
h_s = enthalpy of species s, m^2/s^2
k = Boltzmann constant, J/K
M = Mach number
m_s = mass of species s, kg
n_s = number of species
Q_{catal} = catalytic integrated heat load, J/cm^2
Q_{tot} = total integrated heat load, J/cm^2
q_{cond} = conductive heat flux, W/cm^2
q_{conv} = total convective heat flux, W/cm^2
T_{rec} = recovery temperature, K
T_w = wall temperature, K
T_∞ = freestream temperature, K
t = time, s
t_{bar} = one-dimensional heat capacity of the structure, m
α = angle of attack, deg
γ_s = fraction of species s recombined on surface
ϵ = surface emissivity
η = normal direction component
κ = gas thermal conductivity, W/m-K
κ_{solid} = solid thermal conductivity, W/m-K
ρ = mixture density, kg/m^3
σ = Stefan–Boltzmann constant, W/cm^2 K^4

Introduction

THE purpose of the X-33 program is to build a subscale, suborbital, fully reusable single-stage-to-orbit (SSTO) rocket that will serve as a technology demonstrator for a larger reusable launch vehicle (RLV). The major goal of the RLV program is to dramatically reduce the costs of putting payloads into low Earth orbit. A brief recent history of the RLV program is as follows. Early work related to the X-33 program began with the access to space study.[1] In Ref. 1, some of the benefits of an SSTO were illustrated. Reference 1 led to the RLV technology development program. The purpose of the RLV technology program was to address key technology development issues such as new thermal protection systems (TPS), cryotanks, composite structures, and propulsion related to RLVs. In parallel, phase I for X-33 was a 14-month study. In X-33 phase I, three SSTO vehicle concepts were studied: 1) a lifting body (Lockheed Martin), 2) a winged body (Rockwell), and 3) a vertical takeoff and lander (McDonnell Douglas). After the completion of the phase I studies, a contract was awarded to build and flight test an X-33 vehicle. The winning concept was the lifting body developed by Lockheed Martin.

The work in this paper describes the trajectory-based TPS sizing generated for Rockwell's winged-body concept in X-33 phase I. To capture the heating pulse, the suborbital trajectory with a peak Mach number of 14.72 is discretized at eight points. A material map, employing a tile nosecap and wing leading edges and various flexible ceramic blankets, is generated, and three-dimensional, chemically reacting, laminar, Navier–Stokes flow solutions are calculated at each trajectory location; further, fully turbulent flow solutions are calculated at five trajectory points. The aerothermal database generated from the trajectory calculations with appropriate TPS stackups is used as input for one-dimensional conduction analysis and sizing program. A baseline TPS sizing is performed, and weights for the various TPS components are predicted. Finally, with the turbulent calculations, the TPS weight growth as a function of transition to turbulence is estimated.

The work in this paper is important to the RLV program for a number of reasons. First, the methodology used is being applied to the Lockheed lifting-body design in phase II of the X-33 program. The methodology was applied to a lifting-body[2] concept in the RLV technology development program but not as part of Lockheed phase I activities. Thus, lessons learned in this study about the overall methodology will be useful for phase II activities. Second, flexible ceramic blankets of some type are likely to be used on X-33, RLV, and other future space transportation vehicles; the present study illustrates the application of blanket technology for a number of blanket concepts in an X-33 flight environment. Third, a tile nosecap and leading edges are proposed for X-34. The present X-34 is a winged-body concept being designed by Orbital Science Corporation, which is similar to Rockwell's X-33 winged-body concept; the X-34 vehicle, however, is smaller and the peak Mach number for X-34 is Mach 8, which is much lower than peak Mach number for X-33. Finally, the effects of turbulent transition on TPS design and weight growth will be a critical issue for both X-33 and RLV.

The TPS sizing methodology employed in this study was developed as part of the RLV technology development program; during the program, the methodology was applied to lifting-body,[2] winged-body,[3] and vertical takeoff and lander[4] vehicle concepts. Numerical aspects of the flow solution methodology, sizing procedure, and fluid–TPS coupling strategy used in Refs. 2–4 are described in Refs. 5 and 6. In Ref. 7, the fidelity of the TPS sizing methodology was examined by comparing with the STS-2 flight data.[8] Quantities necessary for TPS design, surface temperatures and heating, bondline temperature, integrated heat loads, and TPS thicknesses, were

Received April 30, 1997; revision received Nov. 19, 1997; accepted for publication Nov. 24, 1997.

*Research Scientist, Reacting Flow Environments Branch, MS 230-2. Senior Member AIAA.

Table 1 TPS material properties

Material	Temperature use range, K	Emissivity	Catalycity
FRSI	$T < 644$	0.80 (Ref. 23)	RCG coating[22]
AFRSI	$644 < T < 1366.5$	White C-9 coated quartz fabric[23]	Nicalon silicon carbide TABI[23]
TABI	$1088.7 < T < 1366.5$	White C-9 coated quartz fabric[23]	Nicalon silicon carbide TABI[23]
TUFI	$1366.5 < T < 1644.3$	0.85 (Ref. 22)	TUFI coating[22]

numerically predicted and compared with the Shuttle flight data; for the windside thermocouples, the comparison was good. Finally, grid generation, structure, and resolution are important factors when using three-dimensional Navier–Stokes solvers to predict surface heating. The grid generation approach employed in this study is described in Ref. 9.

Finally, an important issue in the RLV program is traceability. An objective of the RLV program is to develop and demonstrate technologies on the subscale, suborbital X-33 vehicle that address the technology needs of the larger, orbital RLV. Thus, traceability denotes the process of tracing the applicability of technology development and system integration from X-33 to RLV.

Numerical simulation provides one method for establishing traceability. For example, for TPS traceability, the TPS material mapping and sizing performed for X-33 in this study is designed to produce TPS surface and bondline temperatures that are similar to those expected for a RLV. In a companion paper,[10] the TPS material concepts and TPS design methodology used in this work is applied to the Shuttle; Shuttle flow calculations with a new TPS material map are generated for STS-2 trajectory conditions. Thus, the performance of the blanket and tile concepts employed are assessed in a known RLV flight environment further establishing TPS traceability. Issues relating to TPS traceability including results from Ref. 10 pertinent to this work are discussed throughout this paper.

Procedure

Fluid Flow Governing Equations

In this study, a set of governing equations was chosen that is appropriate for an X-33 entry heating environment.[11,12] A set of the Navier–Stokes equations employing finite rate chemistry is solved, including five species equations (N_2, O_2, NO, N, and O), three momentum equations, and one energy equation. The flow is assumed to be in thermal equilibrium. Ionization of NO and N_2 is assumed to be negligible. For the suborbital X-33 trajectory used in this study, these assumptions are reasonable.

The multispecies Navier–Stokes equations described are solved using the finite volume General Aerothermodynamic Simulation Program (GASP) version 2.2 flow solver.[13,14] The implementation of the GASP code allows the user to choose from a large number of numerical modeling and time integration strategies. For calculating blunt-body, entry flow problems,[2–5,7,9,10] the following implementation of the code has been shown to produce good numerical heat transfer predictions, reasonable convergence, and excellent robustness.

The equations are marched in time to steady state using an implicit two-factor approximate factorization scheme in the cross flow planes and employing underrelaxation in the streamwise direction. The upwind fluxes are modeled using a van Leer formulation. A first-order scheme is used in the coordinate directions along and around the body. Normal to the body the scheme is extended to third order using a MUSCL variable extrapolation.[15] The viscous fluxes are approximated using central differences. The finite rate chemistry is modeled using Park's reaction rates.[16]

The various transport properties are calculated using Wilkes semiempirical mixing rule[17] with curve fits for the species viscosities given by Blottner et al.[18] and a constant Schmidt number with Fick's law for the mass diffusion. For the fully turbulent flow calculation, an eddy viscosity is computed algebraically using Baldwin–Lomax.[19] In Ref. 7, fully turbulent flow calculations using the Baldwin–Lomax turbulence model were carried out on the Shuttle and compared with the STS-2 Shuttle flight database. The model was found to qualitatively capture the increase in heating as result of transition to turbulence; further, for some thermocouples the comparison between the predicted turbulent heating and the flight data was good.

TPS Material Concepts: Properties, Mapping, Stackups, and Boundary Conditions

Accurate modeling of the fluid–surface interface for an entry vehicle requires knowledge of the thermal protection materials utilized in the heatshield and their associated properties. For the Rockwell X-33 concept, a number of blanket and tile TPS concepts were employed to generate a TPS material mapping for the vehicle. These TPS concepts include toughened unipiece fibrous insulation (TUFI) tiles for the nosecap and the leading edges, tailorable advanced blanket insulation (TABI), advanced flexible reusable surface insulations (AFRSI), and flexible reusable surface insulations (FRSI). These materials were selected from a large number of candidate TPS concepts after a number of detailed trade studies.[20,21] Some issues considered in the trade studies were weight and performance, and operation, maintenance, acquisition, and technology development costs.

A TPS material map with TUFI, TABI, AFRSI, and FRSI is generated in the following manner. First, a flow solution is generated at peak heating assuming a fully catalytic wall boundary condition with a conservative value for the emissivity; a constant emissivity of 0.75 is used in this study. Next, using the resulting surface temperature distribution, TPS materials are mapped to each surface location using an appropriate temperature range for each TPS material concept. The temperature ranges used in this study are listed in Table 1 (see Refs. 22 and 23). This mapping procedure assumes that peak surface temperature conditions occur at or near peak heating. Generally, this assumption is valid for a RLV type trajectory such as Shuttle because the angle of attack α does not vary much during the heating pulse. For X-33, however, the trajectory is suborbital and α does vary significantly during the heating pulse; when α is small, areas on the upper surface of the X-33 vehicle are more exposed to the flow environment than for the RLV. The validity of the mapping procedure and the impact of α on the mapping are discussed in the Results section. Finally, the temperature ranges of AFRSI and TABI overlap. The maximum use temperature for the AFRSI on the Shuttle, which is constructed from white C-9 coated quartz fabric, is about 886 K. Newer versions of AFRSI with different fabrics and surface coatings permit higher maximum use temperatures. Both TABI and AFRSI are baselined to assess the durability and performance of each system.

The surface emissivity and catalycity values for the TPS materials used are listed in Table 1. The emissivities for TUFI coated tiles and FRSI are assumed constant for the temperature ranges of interest. The emissivity of a white C-9 coated quartz fabric AFRSI blanket is used for the TABI and the AFRSI blankets. For surface catalysis, the surface kinetics of an uncoated Nicalon silicon carbide fabric TABI blanket are assumed for both the AFRSI and the TABI blankets. Thus, the surface properties for the TABI and the AFRSI blankets are identical. The surface kinetics of TUFI coated tiles were determined experimentally. For FRSI, reaction cured glass (RCG) kinetics are assumed.

A number of assumptions are made regarding the surface properties of the TPS materials used. When the flow calculations were generated, surface emissivity and catalysis values were not available for all of the materials baselined. Because these surface properties are needed for the flow simulations and the TPS sizing calculations, values were selected from available data on related TPS materials. The impact and validity of these assumptions is addressed in the following paragraphs.

The TABI and AFRSI blankets baselined for the X-33 vehicle concept employ Nextel 440 fabric face sheets with a white or gray C-9 coating. White C-9 coated blankets are used on the upper surfaces for thermal control; gray C-9 coated blankets, which have a higher emissivity, are used for the windside surfaces to radiate heat away from the surface. For the flow simulations, the emissivity of

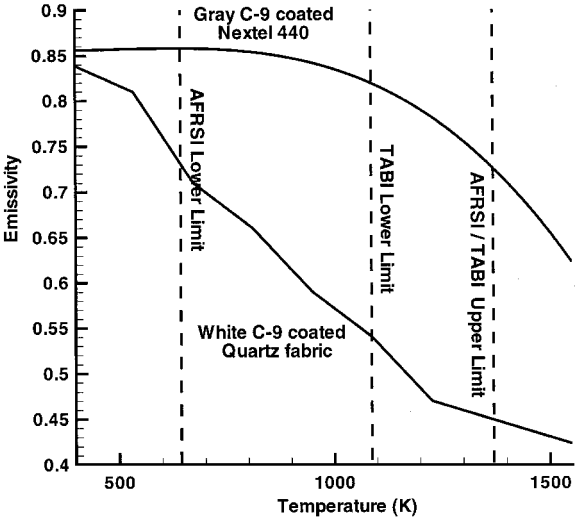

Fig. 1 Comparison of emissivities for gray C-9 coated Nextel 440 and white C-9 coated quartz fabric.

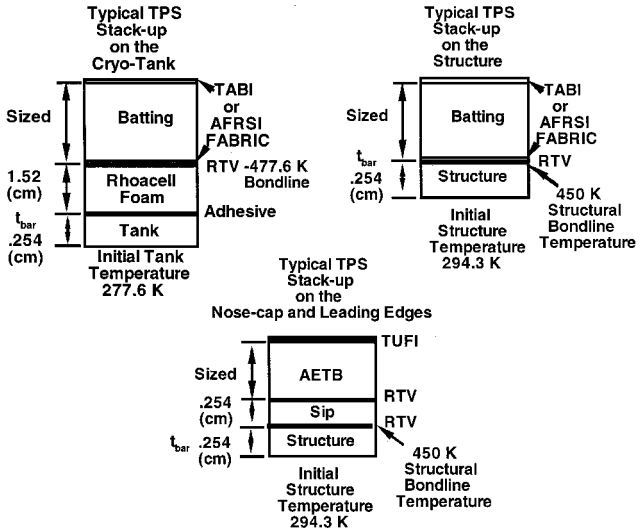

Fig. 2 Typical one-dimensional TPS stackups.

white C-9 coated quartz fabric is used for all of the blankets. The surface emissivity for white and gray C-9 are plotted in Fig. 1; these values became available after the CFD simulations in this study were completed. The temperature use ranges for TABI and AFRSI are also noted. The emissivity values for gray C-9 are much higher than white C-9 in the temperature use ranges for both TABI and AFRSI. Therefore, the surface temperatures calculated in this work for the windside AFRSI and TABI blankets are conservative. In Ref. 10, flow solutions are generated with the blanket material properties used in this study and with the values for gray and white C-9 coated Nextel 440. A comparison of the predicted surface temperatures verifies the conservatism of using white C-9 emissivity values for the windside surfaces.

For the suborbital trajectory used, the fraction of heating from surface catalysis is not large and is limited to the nose region. Thus, although the surface kinetics for gray C-9 coated Nextel 440 and uncoated Nicalon silicon carbide are different, the difference will not significantly impact the results. Finally, the assumption of RCG kinetics for the surface catalysis of FRSI will have a small impact on the heating calculations because surface catalytic effects are negligible for vehicle locations where FRSI is used.

To perform the one-dimensional conduction analysis and TPS sizing, one-dimensional TPS stackups are needed at each surface location. A number of the TPS stackups used are shown in Fig. 2. For this X-33 vehicle concept, integral cryotanks for the H_2 and O_2 propellants are baselined. A carbon composite H_2 tank is at the front of the vehicle and an aluminum-lithium, O_2 tank is above the wings at the rear of the vehicle. In the tank regions, the one-dimensional stackups are TABI, AFRSI, or FRSI bonded to Rhoacell foam; the Rhoacell foam is bonded to the carbon-composite H_2 tank or the aluminum-lithium, O_2 tank. The foam thickness is a constant 1.52 cm at all of the tank locations. For the nosecap, TUFI coated alumina enhanced thermal barrier (AETB-12) tiles are bonded to a Nomex felt strain isolation pad (SIP); the SIP thickness is a constant 0.254 cm and is bonded to a carbon composite structure. On the wing leading edges, TUFI coated AETB-20 tiles are bonded to a 0.254-cm Nomex felt SIP, which is bonded to a carbon composite structure. At the remaining vehicle locations, TABI, AFRSI, or FRSI blankets are bonded directly to the carbon composite structure. The bonding agent used to attach the TPS to the foam, SIP, or structure is room temperature vulcanizing (RTV-560) silicon adhesive; this bonding agent is used to attach the blankets and tiles on the Shuttle.

Other information needed to perform the TPS sizing are initial temperatures of the structure and cryotanks, bondline temperatures, and the effective heat capacitance of the structure and cryotanks. These values are also shown in Fig. 2. The estimated initial temperatures for the cryotanks and structure at the start of the heat pulse are 277.6 and 294.3 K, respectively. The bondline temperature for TPS bonded to the carbon composite structure is 450 K; the TABI or AFRSI batting, TUFI tile, or FRSI is sized to prevent the structure from rising above this temperature. For TPS bonded to Rhoacell foam, the driving temperature for the TPS sizing is the bondline temperature of the RTV adhesive at the TPS/Rhoacell interface; the bondline temperature at this interface is 477.6 K. The temperature at the TPS/Rhoacell interface drives the TPS sizing because the Rhoacell foam insulates the TPS from the cryotank producing a nearly adiabatic boundary condition. Finally, the structure and cryotanks act as heat sink in the TPS sizing calculations. The multidimensional heat capacitance of the structure is represented by an approximate one-dimensional thickness t_{bar} in the sizing, which is usually greater than the actual structural thickness. In this study, the actual structural thickness of 0.254 cm is used, which is conservative.

With the TPS surface properties specified, the boundary conditions at the fluid–TPS interface are determined by solving mass and energy balance equations. The surface energy balance is given as

$$\kappa \frac{\partial T}{\partial \eta} + \sum_{s}^{ns} \left(\rho D h_s \frac{\partial c_s}{\partial \eta} \right) = \epsilon(T_w) \sigma T_w^4 + q_{\text{cond}} \tag{1}$$

where the q_{cond} term is assumed to be zero, which by definition is a radiative equilibrium wall condition. Thus, for the fluid, conduction into the TPS is neglected. Conduction effects, however, are considered when in-depth TPS temperature profiles are calculated; for the solid, the energy balance at the fluid–TPS interface includes the conduction term and the heat transfer from the fluid to the TPS formulated in terms of a heat transfer coefficient and recovery temperature [see subsequent Eqs. (5) and (6)]. These assumptions somewhat decouple the flow and material response calculations. But in Ref. 6 it is shown that these assumptions have a minimal impact on the resulting TPS sizing calculation.

For the mass balance equation, the surface catalysis is modeled using first-order reaction rates. Thus, the mass flux at the wall can be related to the rate of diffusion toward the surface as[24]

$$\left(\rho D \frac{\partial c_s}{\partial \eta} \right)_w = \rho_s \gamma_s \sqrt{\frac{kT_w}{2\pi m_s}} \tag{2}$$

where γ_s is curve fit as a function of temperature as[22]

$$\gamma_s = C \exp(-E/T_w) \tag{3}$$

The conduction into the solid is given by

$$\rho c_p \frac{\partial T}{\partial t} = \frac{\partial}{\partial \eta} \left(\kappa_{\text{solid}} \frac{\partial T}{\partial \eta} \right) = \frac{\partial q_{\text{cond}}}{\partial \eta} \tag{4}$$

The solid, a TPS stackup, is discretized and solutions to this equation are generated using the OMLITS[6] code. The thickness of the TPS is a variable that is determined iteratively to satisfy the bondline temperature constraint of the given TPS stackup.

Table 2 X-33 trajectory points on depressed lob

time, s	Altitude, km	Velocity, km/s	Density, kg/m^3	T_∞, K	Mach	α, deg	Chemical model	Flow type
200	56.8	1.972	4.592×10^{-4}	255.9	6.15	5.42	Perfect gas	Laminar
285	67.4	3.3717	1.18×10^{-4}	266.6	11.17	11.75	Five species	Laminar
338.5	62.3	4.579	2.324×10^{-4}	240.8	14.72	15.77	Five species	Laminar
375	58.5	4.2962	3.74×10^{-4}	251	13.53	36.60	Five species	Laminar/turbulent
425	57.7	3.7786	4.092×10^{-4}	253.3	11.84	36.60	Five species	Laminar/turbulent
515	52.3	2.9556	7.782×10^{-4}	268.3	9.00	34.06	Five species	Laminar/turbulent
615	44.8	2.0973	2.0254×10^{-4}	263.5	6.44	27.57	Perfect gas	Laminar/turbulent
680	39.6	1.5935	4.2415×10^{-4}	249.2	5.04	23.98	Perfect gas	Laminar/turbulent

GASP and OMLITS are coupled in the following manner. The heat transfer from GASP in Eq. (1) is written in terms of heat transfer coefficient as

$$q_{\text{conv}} = \kappa\frac{\partial T}{\partial \eta} + \sum_{s}^{ns}\left(\rho D h_s \frac{\partial c_s}{\partial \eta}\right) = C_T(T_{\text{rec}} - T_w) \qquad (5)$$

In OMLITS, a wall temperature T_w accounting for conduction is generated using the following surface energy balance equation:

$$C_T(T_{\text{rec}} - T_w) = \epsilon(T_w)\sigma T_w^4 + q_{\text{cond}} \qquad (6)$$

This methodology was implemented in Ref. 7 to compare with STS-2 Shuttle bondline thermocouple data. Numerical predictions of the bondline temperatures were usually within 20–30 K of the bondline temperatures measured during the flight.

Results

The X-33 trajectory used for the TPS sizing is shown in Fig. 3. The trajectory, called a depressed lob, is chosen because it produces the maximum expected heat loads. The distance covered during the trajectory is approximately 1650 km, and the length of the heat pulse is about 500 s; in comparison, the Shuttle heat pulse is about 1350 s. The vehicle reaches a peak Mach number of 14.72 at an altitude of about 60 km, 338.5 s after liftoff. At 338.5 s, the main engines cutoff, and the vehicle coasts unpowered to the landing site. Peak heating in the trajectory occurs around 40 s after main engine cutoff at a Mach number of 13.53.

The trajectory is discretized at eight points; flow conditions at these locations are given in Table 2. At the first calculation point, the vehicle is on ascent and the angle of attack is 5.42 deg. The angle of attack peaks at 36.6 deg near peak heating and then decreases to 24 deg near the end of the trajectory. This angle-of-attack profile differs from that of the Shuttle; for the Shuttle, the angle of attack is about 40 deg for most the heat pulse. A Shuttle-like profile is also expected for RLV. Therefore, some upper surface areas are exposed to heating on the X-33 vehicle that would not exposed on a RLV. This issue is important for TPS traceability and does impact the material mapping used in this study.

The material mapping used is generated from a flow solution using a fully catalytic radiative equilibrium wall boundary condition with a constant emissivity of 0.75 at the peak heating trajectory conditions. To simplify the flow calculations, the vertical tail of the vehicle and the end of the body flap are removed. Further, body flap and wing flap deflections are not considered. These conditions are used for all of the flow calculations.

The computational grids used are 124 points along the body, 71 points around the body, and 51 points normal to the surface. The proper grid quality necessary to obtain good heating predictions for this grid resolution is discussed in Ref. 9. As shown in Refs. 7 and 9 via comparisons with the Shuttle flight database, this level of grid resolution is adequate for predicting surface heat transfer.

The numerically predicted surface temperatures at peak heating are used to map the TUFI, TABI, AFRSI, and FRSI onto the vehicle's surface according to their use temperature ranges; these ranges are specified in Table 1. The resulting material map is shown in Fig. 4. The top of the vehicle above the AFRSI/FRSI interface and the top of the wing is covered with FRSI. The various shaded patches denote

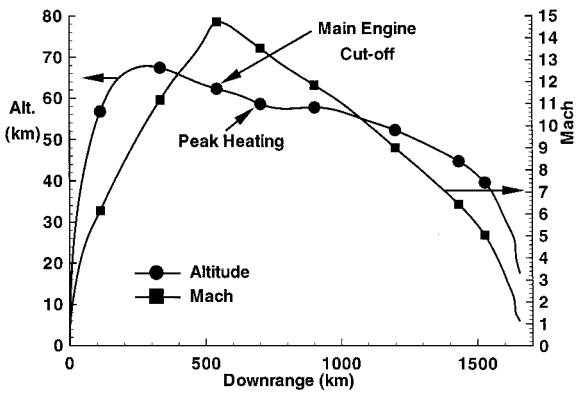

Fig. 3 Trajectory points for the flow calculations.

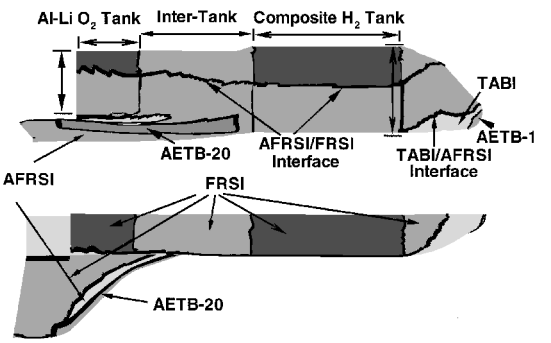

Fig. 4 Material map for sizing computations.

whether the material is on a cryotank or structure; different TPS stackups are used at these locations. For FRSI, the dark patches are on the H_2 and O_2 cryotanks. AETB-20 is used on the wing leading edges and at the wing–body juncture. AETB-12 is used on the nosecap. Between the TABI/AFRSI interface and the AETB-12 is a patch of TABI. Finally, the rest of the vehicle is AFRSI; the patches of AFRSI on the O_2 and H_2 cryotanks are slightly lighter than the other patches of AFRSI.

In the rest of this section, results of the TPS sizing calculation are presented in the following order. First, results of a baseline TPS sizing are presented. Next, the impact on the TPS sizing calculation of uncertainties in predicting turbulent transition are discussed and quantified. Finally, total TPS weights including turbulence effects are described.

For the baseline sizing, flow calculations are generated at each trajectory condition to produce an aerothermal database. Before 515 s, laminar flow is assumed. Based on a transition criterion developed from Shuttle experience, turbulent transition was estimated to occur at Mach 9.0. At the Mach 9.0, 515-s conditions, the flow is assumed to be fully turbulent after the wing–body juncture. At this location, there is a change in surface slope that produces a rise in heating; wind-tunnel data indicate that transition to turbulence is likely at this location. At the 615- and the 680-s conditions, the flow is assumed fully turbulent from the nose. This assumption is consistent with Shuttle flight experience, which shows that the turbulent transition front quickly moves up the vehicle toward the nose.[8,25] For

comparison, laminar flow solutions are also generated. In summary, the baseline trajectory refers to laminar flow before 515 s, mixed laminar and turbulent flow at 515 s, and fully turbulent flow from the nose after 515 s.

The database produced from the baseline TPS sizing is quite large. Flow quantities are available at each grid point for 12 flow calculations. Some quantities in the database relevant to the sizing calculation are surface temperature, pressure, heat transfer vs time, integrated heat loads, TPS thicknesses, and in-depth temperature profiles vs time at each of the 8610 (123 × 70) surface locations. Thus, to present the maximum amount of information, most of figures discussed in this section show database quantities plotted over the surface of the vehicle. However, to illustrate the local information that is available, data are presented at two surface locations: the stagnation point and a point at the wing–body juncture on the windward centerline.

Figure 5 is a plot of surface heat transfer, catalytic heat transfer, and surface temperature vs time for the baseline and laminar trajectory calculations at the stagnation point; the TPS material at this location is a TUFI tile, and a radiative equilibrium wall boundary condition is used. The surface catalytic heat transfer denotes the component of heat transfer resulting from the recombination of N and O on the surface. The total heat transfer q_{tot} is the sum of the convective and catalytic heat transfer components. The effects of transition to turbulence are minimal. At the 338.5-, 375-, and 425-s trajectory conditions, the catalytic component of the surface heat transfer is significant; the catalytic fraction of the integrated heat load is about 25% of the total. The peak temperature at the stagnation point is about 1470 K, which is well below the maximum TUFI temperature of 1650 K. Figure 6 is a plot of surface heat transfer, catalytic heat transfer, and surface temperature vs time for the baseline and laminar trajectory calculations at the wing–body juncture on the windward centerline; the TPS material at this location is an AFRSI

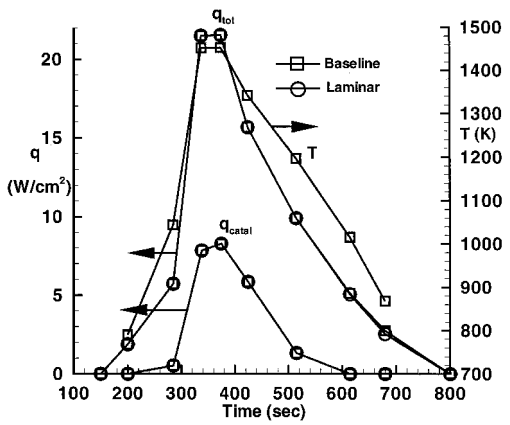

Fig. 5 Temperature and heating profiles vs time at the stagnation point; TUFI tile: radiative equilibrium wall boundary condition.

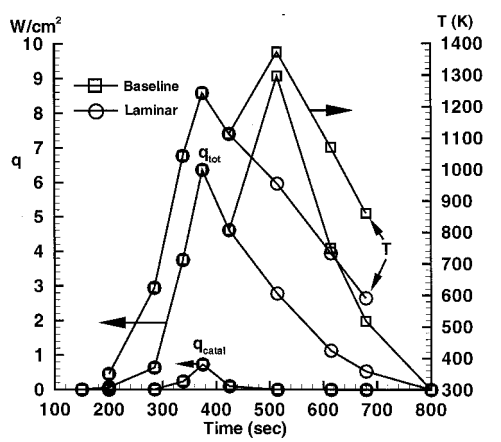

Fig. 6 Temperature and heating profiles vs time at the wing–body juncture; AFRSI blanket: radiative equilibrium wall boundary condition; windside centerline, x = 17.15.

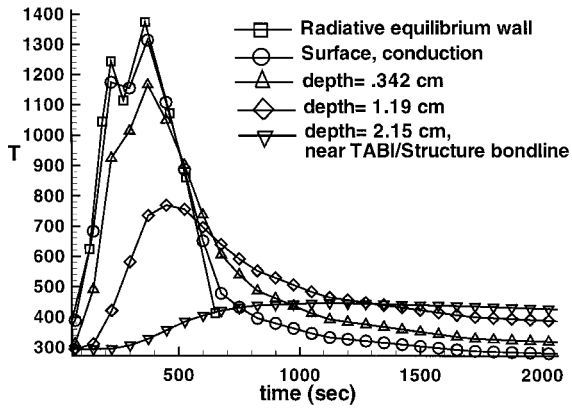

Fig. 7 In-depth temperature profiles vs time at the wing–body juncture; AFRSI blanket: thickness = 2.13 cm; windside centerline, x = 17.15 m.

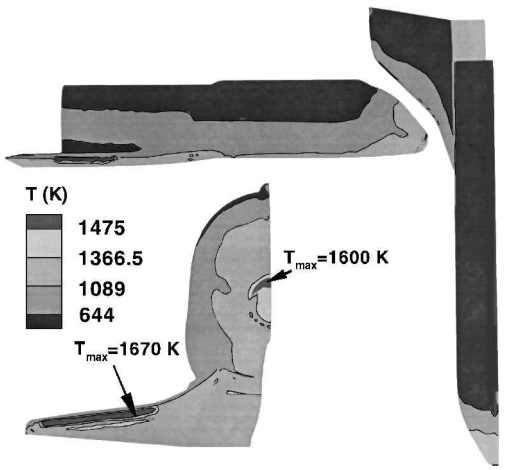

Fig. 8 Maximum surface temperatures over the trajectory.

blanket. For this point, the effects of turbulent transition are significant; the heat transfer at 515 s is more than three times the laminar value. The integrated heat load is nearly doubled, which increases the TPS thickness. The transition to turbulence at 515 s produces a surface temperature that is almost over the maximum use temperature for the AFRSI blanket of 1366 K. This temperature, however, is conservative because of the low white C-9 emissivity value used for the blanket (see Fig. 1). Finally, the catalytic fraction of the total heat transfer is negligible at this point.

Figure 7 is a plot of the surface and in-depth temperature profiles vs time at the wing–body juncture point. The AFRSI blanket at this point is sized to 2.13 cm by the 450-K TPS-structural bondline temperature limit. The maximum surface temperature with conduction into the blanket is about 50 K lower than the maximum surface temperature using a radiative equilibrium wall boundary condition. The bondline temperature continues to rise after end heat pulse because of the heat soak into the blanket; the maximum bondline temperature occurs about 500 s after the end of the heat pulse.

In the next set of figures, quantities relevant to the TPS sizing are plotted over the surface of the vehicle. Figure 8 is a plot of the maximum surface temperature at each surface location during entry for the baseline trajectory calculation; the conduction effects are included. The largest surface temperatures occur on the TUFI wing leading edge; the maximum value is 1670 K, which is slightly above the TUFI use limit. Near the nose, the largest temperatures occur on the TABI blankets just above the TUFI nosecap. The high temperatures at this location are a result of two factors. First, the emissivity used for the TABI blanket is much lower than the TUFI tiles, which causes a jump in temperature. Second, at the 338.5-s conditions, the heat transfer rate is nearly equal to the peak heating value (see Fig. 5), but the angle of attack is less than half the peak heating value. Thus, the surface heat transfer to the area above the nosecap is increased. As discussed earlier, the material mapping based on a

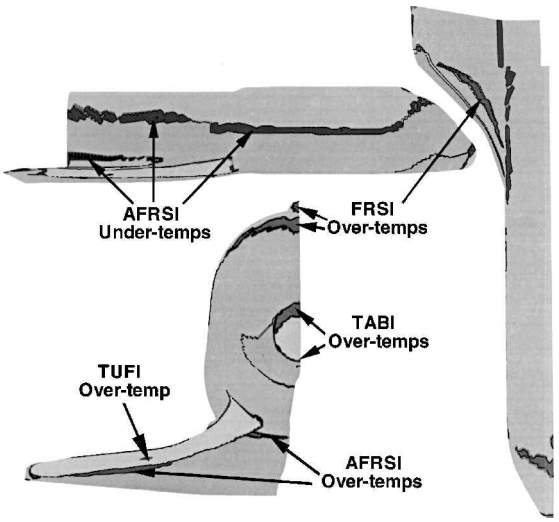

Fig. 9 Validity of material mapping.

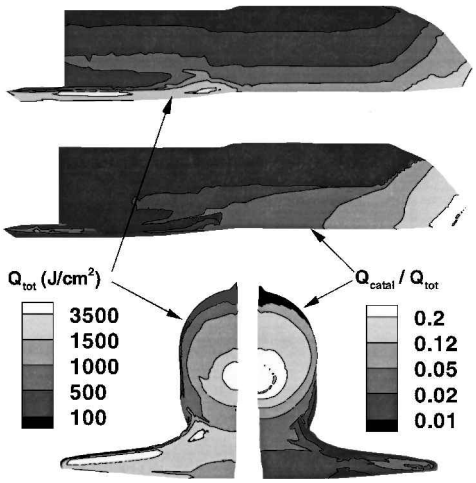

Fig. 10 Total integrated heat load and the catalytic fraction of the integrated heat load.

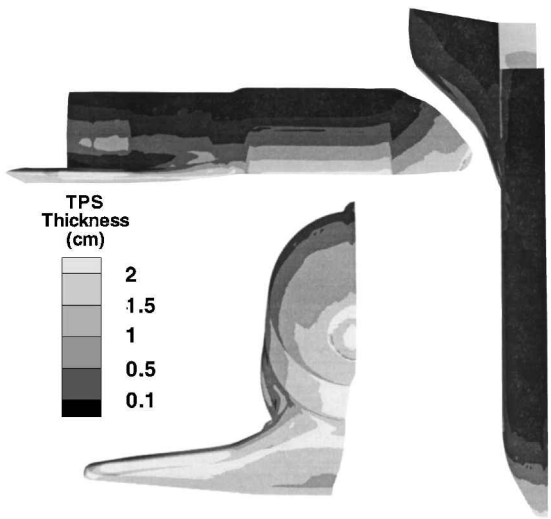

Fig. 11 Surface TPS thickness distribution.

flow calculation at peak heating conditions does not capture this effect. For RLV, this angle-of-attack effect is not expected because the angle of attack is a relatively constant value throughout the pulse. Other features noted in Fig. 8 are an increase in temperature on the side of the body above the wing as a result of a vortex emanating at the wing–body juncture and an increase in temperature as a result of an increase in surface slope at the wing–body juncture.

To check the validity of the material mapping procedure, the maximum and minimum surface temperatures are compared with the temperature use range of the TPS material at each surface location; in Fig. 9, surface locations where the material map is invalid are noted. Above the nosecap, the TABI temperature use range is exceeded as a result of the lower angle of attack at 338.5 s. On top of the wing and above the nosecap near the top of the vehicle, the FRSI temperature use range is also exceeded as a result of the lower angle of attack at 338.5 s. On the windside surfaces, the AFRSI temperature use range is exceeded at the wing–body juncture and below the wing leading edge as a result of turbulent heating and the low emissivity value used for AFRSI; using the actual emissivity values for the blankets, the temperature limit is not exceeded. On the wing leading edge, the temperature use range of TUFI is slightly exceeded. Finally, around the edges of the AFRSI blankets on the side of the vehicle, two small strips are identified where the temperatures are low enough to use FRSI instead of AFRSI.

The TPS material map is easily adjusted to account for the areas where the map is invalid; TABI is replaced with TUFI above the nosecap, FRSI is replaced with AFRSI on top of the wing and near the top of the vehicle above the nosecap. For the wing leading edge, a material with a higher upper temperature range such as carbon-carbon is needed or the trajectory must be modified to lower the peak heating rate. Finally, the fraction of the total surface area where the mapping is invalid is small. Thus, it is concluded that the mapping procedure used in this study is a good method for generating a TPS map.

The integrated heat load and catalytic fraction of the integrated heat load are plotted in Fig. 10. The largest heat loads are on the nose and wing leading edges. The maximum heat load on the nose is about 5000 J/cm^2. On the wing leading edges, the largest heat loads vary from 7000 to 9500 J/cm^2. On the upper surface and sides, the heat loads are nearly negligible. On the windward surface, a large increase in the heat load occurs at the wing–body junction. To simplify the construction of the X-33 vehicle, the wings were designed to attach to a circular cross section fuselage. At the wing attachment point, the surface slope relative to the flow increases. This change in slope compresses the flow and increases the surface heating. The results from this study show that the savings in construction costs must be balanced against increased aeroheating, which increases the TPS mass and costs.

In Fig. 10, the catalytic fraction of the heat load is above 20% on the nose with a maximum of about 25%. From the nose, the catalytic fraction drops to between 12 and 20% and then to between 5 and 12%. On the top of the vehicle, the catalytic fraction is negligible. On the wings, the catalytic fraction is only about 1–2%. For X-33, the surface distribution of the catalytic fraction of the integrated heat load is significantly different than for the Shuttle.[10] For the Shuttle, the predicted fraction is between 5 and 10% on most of the windside surface, between 10 and 20% on the leading edges, and as high as 40% near the stagnation point. Thus, the X-33 flight environment will capture some catalytic effects, but the fraction of the catalytic heat load is underpredicted relative to a RLV flight environment. At the TPS material interfaces, if the surface catalytic properties vary across the interface, then a temperature jump will occur; the magnitude of the temperature jump is a function of the magnitude of the catalytic heating at the interface and differences in surface catalycity and emissivity between the materials.[5,10] These temperature spikes produce thermal stresses, which are important for TPS design. Thus, in terms of traceability, the underprediction of catalytic effects will have to be accounted for when the X-33 vehicle is scaled to a RLV. Further, as shown in Fig. 5, the catalytic heating only occurs at the higher Mach numbers; therefore, to capture any of these catalytic effects, the vehicle must be flown at Mach 12.0 or higher for a significant fraction of the heat pulse.

In Fig. 11, the TPS thickness distribution is plotted for the baseline TPS sizing. The TPS is thickest on the nosecap, at the base of the H_2 cryotank, on and below the wing leading edges, and at the wing–body juncture. These regions correspond to the areas with the highest heat loads except for the H_2 cryotank. On the cryotank, the TPS thickness increases because the Rhoacell foam insulates the TPS from the structure; for nontank regions, the structure acts as a heat

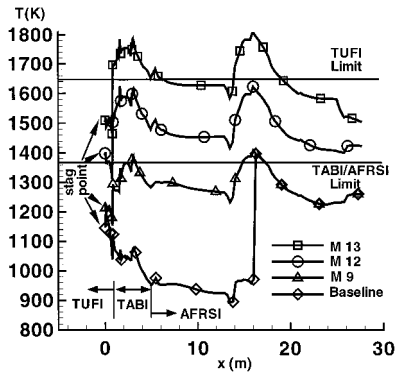

Fig. 12 Windward centerline temperatures for various transition to turbulence assumptions: windward centerline radiative equilibrium boundary condition.

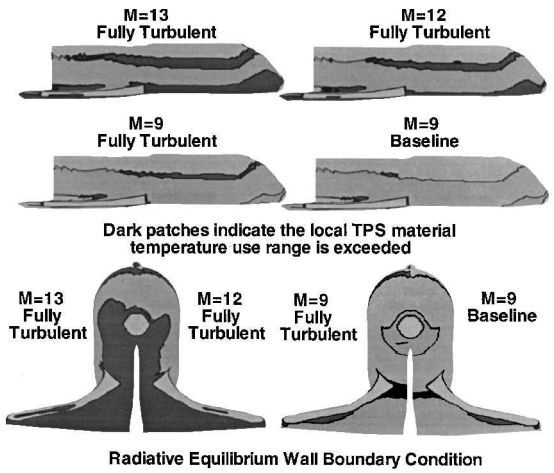

Fig. 13 Effect of transition to turbulence on the TPS material mapping.

sink, which reduces the needed TPS mass. To produce a smooth outer mold line, the increase in TPS thickness on the cryotank must be accounted for in the vehicle's design. On the upper surface, the heat loads are minimal and minimum gauge FRSI is used.

The effects of turbulence are assessed by assuming transition to turbulence at various points in the trajectory. For the baseline calculations, transition to turbulence is assumed at the wing–body juncture for the Mach 9 flow conditions. Three other turbulent calculations are generated: fully turbulent from the nose for Mach 9, fully turbulent from the nose for Mach 11.73, and fully turbulent from the nose for Mach 13.53, which is peak heating. In Fig. 12, a comparison of the radiative equilibrium wall temperatures along the windward centerline for the turbulent flow calculations is shown; also, the locations of the three TPS materials, TUFI, TABI, and AFRSI, used along the windward centerline are shown. For the baseline calculation, the temperature rises 400 K at the wing–body junction where fully turbulent flow is assumed; the TABI/AFRSI temperature limit is slightly exceeded at this point. For the Mach 9 calculation, the jump at the wing–body juncture is smaller because fully turbulent flow is assumed from the nose. Near the stagnation point, the temperature increases significantly at the TUFI/TABI interface because the emissivity used for TABI is much lower than TUFI and as a result of turbulent heating. Large local surface temperature jumps increase the thermal stress within the structure[5]; these jumps are a factor when the structure is designed.

For the Mach 12 and 13 calculations, the TABI/AFRSI temperature limit is exceeded along the entire windward centerline. Thus, if early transition is assumed for the baseline design, then tiles are needed over much of the windward surface. For the Shuttle, early transition, near peak heating, has been observed on a few flights.[25] Because the TABI emissivity is much lower than the TUFI emissivity, the jump in temperature at the TUFI/TABI interface is about 200 K. Using a higher emissivity coating for the blankets such as the gray C-9 (see Fig. 1), fewer tiles would be needed to account for transition to turbulence at the Mach 12 conditions. For transition to turbulence at peak heating, however, the AFRSI and TABI blankets are not suitable for the high heating areas on the windside surface, and tiles are required. Thus, a major impact of turbulent heating is a change in the TPS material map; in general, the cost and weight of a material is proportional to its operational temperature range. For example, tiles are more expensive and heavier and cost more to maintain than AFRSI or TABI blankets. The costs associated with AFRSI or TABI are higher than FRSI.

In Fig. 13, the effect of turbulent heating on the TPS material map over the vehicle is shown for the four transition assumptions shown in Fig. 12. In Fig. 9, the validity of the TPS map is displayed at each surface location; the maximum use temperature for each material is compared with predicted surface temperatures over the entire trajectory. In Fig. 13, to separate the effects of turbulence, the maximum TPS use temperature at each surface location is compared only with the predicted radiative equilibrium wall temperature generated at the indicated flow condition. In Fig. 13, the dark patches indicate regions where the local TPS temperature use range is exceeded.

For the baseline calculation, material temperature limits are exceeded below the wings and for a few small regions on the side of the vehicle. For the Mach 9 turbulent assumption, the region on the side of the vehicle where the TPS material limits are exceeded grows and extends to the front of the vehicle, and the temperature limit of TABI near the nose is exceeded in a small area. For the Mach 12 and 13 turbulent assumptions, most of the windside TPS materials are above their temperature limit, the areas on the side and front of the vehicle grow, and a patch of tiles on the wing leading edge is above the TUFI material limit.

Finally, TPS weights for five trajectory combinations are generated and tabulated in Table 3. The five trajectory combinations are as follows: all laminar, baseline, fully turbulent from the nose at Mach 9 conditions and after, fully turbulent from the nose at the Mach 11.84 conditions and after, and fully turbulent from the nose at Mach 13.53 and after. The material map described in Fig. 4 is used for all of the calculations. For the last two trajectory combinations, the material map is violated for large areas of the vehicle's surface. Therefore, the TPS sizing results from these calculations are for qualitative purposes only. A more appropriate material map would require heavier TPS materials; thus, the TPS weight for the Mach 11.84 and the Mach 13.53 sizings is underpredicted.

Table 3 shows TPS weights for each material, the total area that each material covers, the average TPS thickness, the weight of the RTV and SIP, and the average weight per area for the entire vehicle. TPS weights for the fin and parts of the body flap are not included. Formulas for calculating the weights and average thicknesses are given in Ref. 26.

In this study, TPS weights are calculated using the unsmoothed output from the one-dimensional sizing. For use on an actual vehicle, additional TPS would be added to produce a smooth outer mold line from the jagged one-dimensional TPS sizing output. Additional TPS is required because TPS panels are generally a constant thickness, and local TPS maximum thicknesses must be maintained to satisfy the bondline temperature constraint. The increased TPS thicknesses add weight and margin to the system.

In Table 3, AFRSI blankets, which cover the most area on the vehicle, are the largest TPS weight component, followed by the weights of RTV, FRSI, AETB-20, TABI, AETB-12, and the SIP. The weights of RTV and the SIP are a function only of area; thus, their weights do not increase with heat load. The total TPS areal density, which is the total weight of the TPS including RTV and SIP divided by the total area, increases by 25% between the laminar and the Mach 13.53 fully turbulent sizing calculations. The maximum TPS areal density for the fully turbulent calculation (2.77 kg/m^2) is about 50% of the value (5.38 kg/m^2) predicted for the RLV type calculation in Ref. 3 and 79% of the value (3.51 kg/m^2) predicted for a Shuttle remapped with the same TPS concepts used in this study[10]; the lower TPS areal density for X-33 vs RLV is another traceability issue.

The TPS components most affected by turbulent heating are the TABI and AFRSI blankets; the average TABI blanket thickness increases by about 70% and the average AFRSI blanket thickness increases by about 85%. The maximum blanket thicknesses are still

Table 3 Weights generated from the TPS sizing calculations

Material	Area, m^2	Weight, kg	Δ_{thick}, cm
Laminar (2.24-kg/m^2 areal density)			
FRSI	197.9	127.6	0.407
AFRSI	281.3	693.2	0.99
TABI	14.1	44.5	1.51
AETB-12	2.1	6.9	1.72
AETB-20	25.7	56.2	0.685
Subtotal	521.1	928.4	——
RTV	521.1	231.9	——
SIP	27.8	6.1	——
Total	——	1166.4	——
Baseline (2.46-kg/m^2 areal density)			
FRSI	197.9	128.6	0.412
AFRSI	281.3	792.1	1.35
TABI	14.1	48.1	1.74
AETB-12	2.1	7.24	1.80
AETB-20	25.7	68.1	0.828
Subtotal	521.1	1044.2	——
RTV	521.1	231.9	——
SIP	27.8	6.1	——
Total	——	1282.1	——
Turbulent $M = 9$ (2.52-kg/m^2 areal density)			
FRSI	197.9	130.5	0.424
AFRSI	281.3	815.4	1.44
TABI	14.1	52.4	2.01
AETB-12	2.1	7.42	1.85
AETB-20	25.7	68.9	0.838
Subtotal	521.1	1074.7	——
RTV	521.1	231.9	——
SIP	27.8	6.1	——
Total	——	1312.7	——
Turbulent $M = 11.84$ (2.65-kg/m^2 areal density)			
FRSI	197.9	132.0	0.432
AFRSI	281.3	874.0	1.65
TABI	14.1	56.8	2.29
AETB-12	2.1	7.56	1.88
AETB-20	25.7	72.1	0.877
Subtotal	521.1	1142.5	——
RTV	521.1	231.9	——
SIP	27.8	6.1	——
Total	——	1380.5	——
Turbulent $M = 13.53$ (2.77-kg/m^2 areal density)			
FRSI	197.9	133.5	0.441
AFRSI	281.3	927.1	1.84
TABI	14.1	60.7	2.54
AETB-12	2.1	7.67	1.91
AETB-20	25.7	76.40	0.929
Subtotal	521.1	1205.4	——
RTV	521.1	231.9	——
SIP	27.8	6.1	——
Total	——	1443.4	——

within the limits of manufacturability for TABI and AFRSI. This result differs from the winged-body RLV type calculation in Ref. 3. In Ref. 3, it is shown that the temperature limits of the blankets are exceeded as a result of transition to turbulence, which agrees with present study. The blanket thicknesses for TABI, however, are beyond the manufacturability limits. Thus, TPS manufacturability is a traceability issue that may not be addressed with this X-33 vehicle concept.

Finally, the weight increase between the baseline sizing calculation and the Mach 13.53 fully turbulent sizing is 161 kg. Thus, for the winged X-33 concept, the major impact of turbulent heating is on the TPS material mapping. For early transition to turbulence, more tiles and possibly reinforced carbon-carbon are required to meet the increased maximum surface temperatures associated with turbulent heating. Tiles are heavier and more costly to obtain and maintain than blankets. Carbon-carbon is heavier than tiles and is very expensive.

Concluding Remarks

A trajectory-based TPS sizing was implemented for an X-33 winged-body vehicle concept. The heat pulse was discretized at eight points along the suborbital trajectory. A TPS material mapping was developed based on predicted surface temperatures at peak heating. Laminar, three-dimensional Navier–Stokes flow calculations were generated at all of the trajectory conditions, and turbulent flow solutions were generated at five of the trajectory conditions using surface mass and energy balances appropriate for the vehicle's TPS material map. With the aerothermal database generated from the Navier–Stokes calculations and one-dimensional TPS stackups that are representative of the TPS and structure at each surface location, a number of TPS sizing calculations were generated.

It is concluded that the TPS mapping procedure works well. For a baseline trajectory that included both laminar and turbulent calculations, the mapping procedure produced a TPS material map that was within the upper and lower TPS operational temperature limits for nearly the entire vehicle's surface. The TPS mapping was violated in a few areas as a result of the lower angle of attack during the suborbital X-33 trajectory and from transition to turbulence.

Four issues of TPS traceability between the X-33 and RLV were identified. First, the angle-of-attack profile for suborbital X-33 trajectory exposes the X-33 TPS to a different heating environment than for RLV; areas on the upper surface of X-33 are exposed to higher heat loads than RLV because the angle of attack during the X-33 heat pulse is lower. Second, the catalytic fraction of the integrated heat load is much lower for X-33 than RLV for much of the windside surface and along the wing leading ledges. Significant catalytic heating occurs above Mach 12; thus, to capture any catalytic heating effects, the X-33 vehicle must fly above Mach 12 for a relevant portion of the heat pulse. Third, the average TPS areal density for X-33 is about half the value for a comparable RLV concept. Fourth, TPS manufacturability issues observed for a similar RLV calculation, the TPS blankets becoming too thick to manufacture, were not demonstrated for X-33.

Finally, a number of turbulent flow solutions were generated assuming fully turbulent flow after the peak heating point in the trajectory. These turbulent flow solutions were combined with the laminar flow solutions to generate a number of TPS sizings. For the X-33 concept in this study, the major impact of early transition to turbulence are higher maximum surface temperatures, which invalidate the TPS material mapping. Higher maximum surface temperatures require heavier and more expensive TPS materials.

Acknowledgments

The author would like to thank Carl Ehrlich, Richard Mongan, Charlie Patrilla, and Willy Mas of Rockwell Space Systems Division for their support on this work. Special thanks to Kurian Mani of Rockwell for providing the initial surface grid and to Dan Dominik of Rockwell for coordinating the computational effort and reviewing the paper. D. A. Stewart of the Thermal Protection Material Branch, NASA Ames Research Center, made available surface emissivity values for white and gray C-9 (August 1996).

References

[1]"Access to Space, Advanced Technology Team, Final Report: Volumes 1-4," NASA, July 1993.

[2]Palmer, G. E., Henline, W. D., Olynick, D. R., and Milos, F. S., "High-Fidelity Thermal Protection System Sizing of Reusable Launch Vehicle," *Journal of Spacecraft and Rockets*, Vol. 34, No. 5, 1997, pp. 577–583.

[3]Henline, W. D., Palmer, G. E., Milos, F. S., Olynick, D. R., and Chen, Y.-K., "Aerothermodynamic Heating Analysis and Heatshield Design of an SSTO Rocket Vehicle for Access-to-Space," AIAA Paper 95-2079, June 1995.

[4]Chen, Y.-K., Henline, W. D., Olynick, D. R., and Palmer, G. E., "Three-Dimensional Hypersonic Flowfields and Heating Analysis over the DC-3 Vehicle," AIAA Paper 95-2081, June 1995.

[5]Olynick, D. R., and Henline, W. D., "Navier–Stokes Heating Calculations for Benchmark Thermal Protection System Sizing," *Journal of Spacecraft and Rockets*, Vol. 33, No. 6, 1996, pp. 807–814.

[6]Chen, Y.-K., and Milos, F. S., "Solution Strategy for Thermal Response of Nonablating Thermal Protection Systems at Hypersonic Speeds," AIAA Paper 96-0615, Jan. 1996.

[7]Olynick, D., and Tam, T., "Trajectory-Based Validation of the Shuttle Heating Environment," *Journal of Spacecraft and Rockets*, Vol. 34, No. 2, 1997, pp. 172–181.

[8]Hartung, L. C., and Throckmorton, D. A., "Space Shuttle Entry Heating Data Book, Volume I: STS-2," NASA Rept. 1191, Pts. 1 and 2, May 1988.

[9]Olynick, D., "Importance of 3-D Grid Resolution and Structure for Calculating Reentry Heating Environments," AIAA Paper 96-1857, June 1996.

[10]Tam, T., and Olynick, D., "Investigation of Possible Shuttle Upgrades Using Advanced TPS Concepts," AIAA Paper 97-0277, Jan. 1997.

[11]Gnoffo, P. A., Weilmuenster, K. J., and Alter, S. J., "Multiblock Analysis for Shuttle Orbiter Re-entry Heating from Mach 24 to Mach 12," *Journal of Spacecraft and Rockets*, Vol. 31, No. 3, 1994, pp. 367–377.

[12]Gnoffo, P. A., Gupta, R. N., and Shinn, J. L., "Conservation Equations and Physical Models for Hypersonic Air Flows in Thermal and Chemical Nonequilibrium," NASA TP-2867, Feb. 1989.

[13]Walters, R. W., Cinnella, P., and Slack, D. C., "A Status Report on GASP—A General Aerodynamic Simulation Program," Seventh National Aero-Space Plane Symposium, Paper No. 9, NASA Lewis Research Center, June 1989.

[14]McGrory, D. M., Slack, D. C., Applebaum, M. P., and Walters, R. W., "GASP Version 2.2: User's Manual," AeroSoft, Inc., Blacksburg, VA, 1993.

[15]Hirsch, C., *Numerical Computation of Internal and External Flows, Vol. 2: Computation Methods for Inviscid and Viscous Flows*, 1st ed., Wiley, New York, 1990, pp. 493–583.

[16]Park, C., "Review of Chemical–Kinetic Problems of Future NASA Missions, I: Earth Entries," *Journal of Thermophysics and Heat Transfer*, Vol. 7, No. 3, 1993, pp. 385–398.

[17]Wilke, C. R., "A Viscosity Equation for Gas Mixtures," *Journal of Chemical Physics*, Vol. 18, No. 4, 1950, p. 517.

[18]Blottner, F. G., Johnson, M., and Ellis, M., "Chemically Reacting Viscous Flow Program for Multi-Component Gas Mixtures," Sandia Labs., Rept. No. SC-RR-70-754, Albuquerque, NM, Dec. 1971.

[19]Baldwin, B. S., and Lomax, H., "Thin-Layer Approximation and Algebraic Model for Separated Turbulent Flows," AIAA Paper 78-257, June 1978.

[20]Ehrlich, C., "Advanced Manned Launch Study (AMLS): Reusable Cryogenic Tank Design," Contract NAS1-18975 DRD-9, Rockwell International, Space Systems Div., Downey, CA, July–Sept. 1993.

[21]"Advanced Structures and TPS Technologies," *Reusable Launch Vehicle Technology Program*, Quarterly Review 1, NASA Marshall Space Flight Center, Huntsville, AL, Oct. 1994.

[22]Stewart, D. A., Pallix, J., and Esfahani, L., "Surface Catalytic Efficiency of Candidate Ceramic Thermal Protection Materials for SSTO," NASA CDTM-20007, March 1995.

[23]Chiu, S. A., and Pitts, W. C., "Reusable Surface Insulations for Reentry Spacecraft," AIAA Paper 91-0695, Jan. 1991.

[24]Park, C., *Nonequilibrium Hypersonic Aerothermodynamics*, 1st ed., Wiley, New York, 1990, p. 141.

[25]Bertin, J. J., Bouslog, S. A., Wang, K. C., and Campbell, C. H., "A Review of Recent Aerothermodynamic Flight Measurements for the Shuttle Orbiter," AIAA Paper 95-0295, Jan. 1995.

[26]Olynick, D. R., "Trajectory Based TPS Sizing for an X-33 Winged Vehicle Concept," AIAA Paper 97-0276, Jan. 1997.

T. C. Lin
Associate Editor